Characterization of single shallow silicon-vacancy centers in 4*H*-SiC

Harpreet Singh [1,2,*] Mario Alex Hollberg [1] Misagh Ghezellou [3] Jawad Ul-Hassan [3]
Florian Kaiser [4,5] and Dieter Suter [1]

[1]*Fakultät Physik, Technische Universität Dortmund, Dortmund D-44227, Germany*
[2]*Department of Chemistry, University of California, Berkeley, Berkeley, California 94720, USA*
[3]*Department of Physics, Chemistry and Biology, Linköping University, Linköping SE-58183, Sweden*
[4]*3rd Institute of Physics and Research Center SCOPE, University of Stuttgart, Stuttgart 70569, Germany*
[5]*Materials Research and Technology (MRT) Department, Luxembourg Institute of Science and Technology (LIST), 4422 Belvaux, Luxembourg*

Shallow negatively charged silicon-vacancy centers have applications in magnetic quantum sensing and other quantum applications. Vacancy centers near the surface (within 100 nm) have different spin relaxation rates and optical spin polarization, affecting the optically detected magnetic resonance (ODMR) signal. This makes it essential to characterize these centers. Here we present the relevant spin properties of such centers. ODMR with a contrast of up to 6%, which is better than the state of the art, allowed us to determine the zero-field splitting, which is relevant for most sensing applications. We also present intensity-correlation data to verify that the signal originates from a single center and to extract transition rates between different electronic states.

I. INTRODUCTION

Silicon vacancies in silicon carbide (SiC) are excellent candidates for quantum sensing and information applications [1–4]. Negatively charged silicon vacancies (V_{Si}^{-}) have spin 3/2 [5,6]. The spin of V_{Si}^{-} can be initialized into a particular spin ground state by optical pumping [4,5,7] and it has sufficiently long coherence and relaxation times for many interesting applications [2,3,8–12]. Debye-Waller factors of about 6% were found for the V_1 and V_2 type of V_{Si}^{-} [13,14], which is vital for the quantum applications that rely on indistinguishable photon emitters. The electronically excited-state zero-field splitting of the V_2 centers in 4*H*-SiC exhibits a significant thermal shift, which makes them useful for thermometry applications [15]. V_{Si}^{-} in SiC provides a low-cost and simple approach to the quantum sensing of magnetic fields and a sensitivity of 50 nT/$\sqrt{\text{Hz}}$, which was achieved without complex photonic engineering, control protocols, or application of excitation (optical and radio-frequency) powers greater than one watt [16]. Absolute dc magnetometry, which is immune to thermal noise and strain inhomogeneity, has been demonstrated using all four ground-state spin levels of V_{Si}^{-} [17]. Similar to NV in diamond, V_{Si}^{-}-based magnetometers can also be applied to unique magnetic sensing challenges, such as resolving an individual nuclear spin in a molecule [18]. Since the magnetic field of a dipole decreases with distance as $1/r^3$, it is essential that the sensor can be brought close to the source [18], which is only possible if the V_{Si}^{-} is close to the surface.

Silicon vacancies can be created, e.g., by irradiating the sample with neutrons or electrons [19–21]. The charge on the silicon vacancy depends on the Fermi level: if it is at least 1.24 eV above the valence band, the *k*-lattice site becomes negatively charged and, at 1.5 eV, the *h*-lattice site also becomes negatively charged [22]. Irradiation by proton or other charged ions allows one to create a plane of vacancies at a specific depth that depends upon the energy and type of the ions [23–25]. Here we focus on single silicon-vacancy centers created with 6 keV He$^+$ ion irradiation. Using a lithographic polymethyl methacrylate (PMMA) mask with 100 nm holes, an array of silicon vacancies was created [23] at a depth of 30–40 nm below the surface. Additional details of the sample preparation are given in Appendix A.

In this work, we focus on the V_{Si}^{-} in the 4*H*-SiC polytype, specifically, V_{Si}^{-} centers at hexagonal sites *h* and cubic sites *k*, which are commonly known as V_1 and V_2 [26]. We characterize the properties of several individual centers and obtain useful values for the optical transition rates as well as for the radiationless population dynamics. We demonstrate that the optical pumping results in spin polarization that is sufficiently high to observe optically detected magnetic resonance (ODMR) spectra of single silicon-vacancy centers at room temperature with high contrast. From a series of ODMR spectra with different RF powers, we could extract the transverse dephasing time.

This paper is organized as follows. Section II introduces the optical and magnetic properties of a single spin system. Section III provides details of the correlation measurement experiments and analysis to estimate the rates involved in the population dynamics of the center during optical excitation. Section IV shows continuous-wave optically detected magnetic resonance (cw-ODMR) experiments at different RF powers. Finally, Sec. V contains a brief discussion and some concluding remarks.

II. SYSTEM AND SETUP

The V_2 center has C_{3v} symmetry and an electron spin $S = 3/2$. In the absence of a magnetic field, the spin
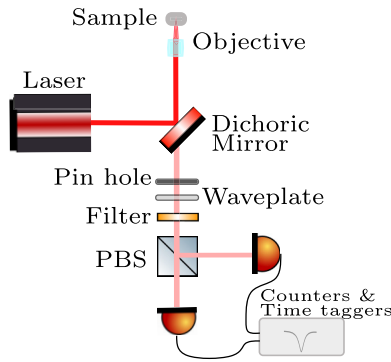
*harpreets@berkeley.edu

FIG. 1. Experimental confocal setup used for PL and intensity-autocorrelation measurements.

Hamiltonian is

$$\mathcal{H} = D\left[S_z^2 - \frac{S(S+1)}{3}\right], \quad (1)$$

where the zero-field splitting (ZFS) in the electronic ground state is $2D = 70$ MHz in frequency units $(h = 1)$ [3,27]. $\vec{S} = \{S_x, \ S_y, \ S_z\}$ is the vector of spin operators and we have chosen the z axis parallel to the c axis of the crystal (C_{3v} symmetry axis).

Figure 1 shows the experimental confocal setup for measuring photoluminescence (PL) and the second-order intensity autocorrelation. A 785 nm laser beam was focused on the sample with an objective lens of numerical aperture (NA) 1.3. With the help of a dichroic mirror, the PL emitted by the sample was filtered and allowed to pass through a $\lambda/2$ waveplate, a set of optical filters, and a polarizing beam splitter (PBS). Two single-photon detectors (SPDs) were used for the two possible paths. With the $\lambda/2$ waveplate, we controlled the ratio of photons detected by these two detectors. From the arrival time of the photons, we calculated the intensity-autocorrelation function $g^{(2)}$. For taking PL scans, the counts of both SPDs were added and plotted against the XY position. For simplicity, some of the mirrors and lenses are not shown in Fig. 8; details are summarized in Appendix A.

Figure 2 shows a confocal PL scan of a part of the sample. The plot shows that most V_{Si}^- centers lead to a photon detection rate of ∼8000 cps (counts/s) at room temperature. Higher count rates are also observed in some locations, indicating multiple close centers. The counts due to impurities and dirt are higher than the counts of the vacancies and usually bleach away after a few minutes of laser illumination.

III. POPULATION DYNAMICS

We measured the second-order correlation function of the PL light emitted by a V_{Si}^-. This allowed us to verify that the light is emitted by a single center as well as to study the population dynamics. The second-order correlation function

$$g^{(2)}(\tau) = \frac{\langle n_1(t) n_2(t+\tau)\rangle}{\langle n_1(t)\rangle\langle n_2(t+\tau)\rangle}$$

is the conditional probability of measuring two photons with a delay τ. Here, $n_i(t)$ are the number of photons detected at
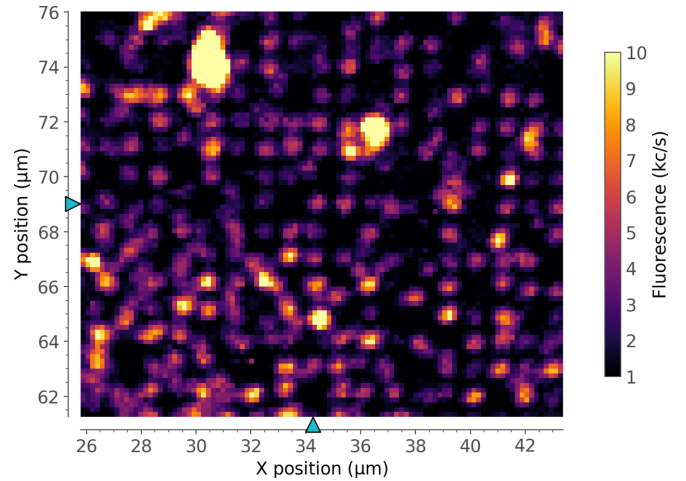

FIG. 2. Confocal scan of the defect center array in the *XY* plane. Large count rates are due to dirt and impurities. The count rate is color coded, and its value can be taken from the bar on the right.

time t [28]. For an ideal single-photon emitter, the conditional probability of detecting two photons simultaneously drops to zero, $g^{(2)}(\tau = 0) = 0$ [28]. Experimentally, $g^{(2)}(0) < 0.5$ is evidence for a single-photon emitter. Figures 3 and 9 show the experimental correlation data. The minimum in the curve is shifted from $\tau = 0$ by $\tau_0 = 1.0 \pm 0.2$ ns, which originates in unequal delays of the optical and electrical detection paths of the two SPDs.

We performed correlation measurements with different laser intensities. Figure 3 shows the intensity autocorrelation vs the delay τ for laser intensities 2.6 kW/cm^2 and 378 kW/cm^2 with orange diamonds and green stars, respectively. The bin width, count rates, and background details used for normalizing the plots are given in Appendix B, along with data for additional laser intensities. Experimental correlation functions with $I < 135$ kW/cm^2, reveal an antibunching dip, indicating that the selected PL source is a single-photon emitter $g^{(2)}(\tau = 0) = 0.17$ for laser intensity $I = 2.6$ kW/cm^2. As
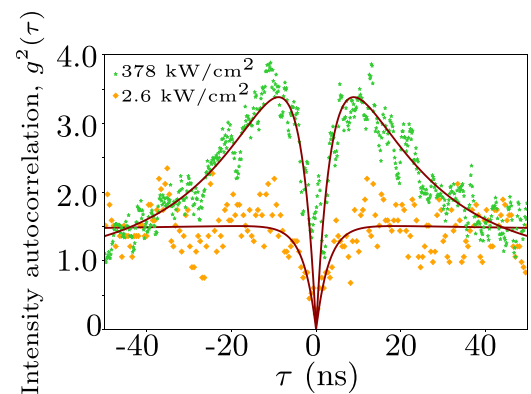

FIG. 3. Intensity-autocorrelation measurements performed with 2.6 kW/cm^2 and 378 kW/cm^2 laser intensity in the focus. In the data recorded with intensity $I = 2.6$ kW/cm^2, the background count rate was negligible, but it was significant for $I = 378$ kW/cm^2. We therefore performed a background correction. Each solid line follows the three-level correlation function from Eq. (5).
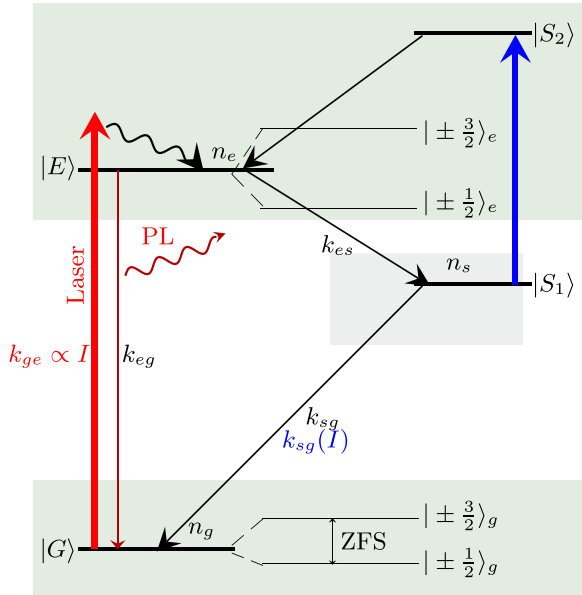
FIG. 4. Electronic energy levels scheme for V_{Si}^- on the cubic site (V_2). The optical excitation with a 785 nm laser, from the ground state to the excited state, is indicated by the thick red arrow. Direct radiative (PL) relaxation from the excited state $|E\rangle$ to the ground state $|G\rangle$ is represented by a thin dark-red arrow. From the excited state, the center can undergo intersystem crossing (ISC) to the shelving state $|S_1\rangle$, as indicated by black arrows. The ground-state spin sublevels are separated by the ZFS. k_{ge}, k_{eg}, k_{es}, and k_{sg} are the transition rates from the ground state to excited state, excited state to ground state, excited state to shelving state, and shelving state to ground state, respectively. The deshelving process corresponds to a transfer of population from $|S_1\rangle$ to a higher-energy level, $|S_2\rangle$, followed by another ISC.

shown in Fig. 10, the signal increases linearly with the laser intensity I for low power, but saturates for $I > 130$ kW/cm^2. The background increases linearly with I, which results in a decreasing signal-to-background ratio at higher powers I and a reduced antibunching dip [$g^{(2)}(\tau = 0) > 0.5$], for data taken at $I > 135$kW/cm^2 (plotted in Fig. 9 in Appendix B [29]. A bunching behavior is observed for $|\tau| > 9$ ns for the laser intensity of 378 kW/cm^2 in Fig. 3.

These data can be modeled by considering at least a three-level system, as shown in Fig. 4. Absorption of laser light brings the system from the ground state $|G\rangle$ to the excited state $|E\rangle$ with a rate k_{ge}, which is proportional to the laser intensity I. Due to spontaneous emission from the excited state $|E\rangle$, most of the population returns to the ground state $|G\rangle$ with a rate k_{eg} and emits PL. Some of the population goes to the shelving state $|S_1\rangle$ due to the intersystem crossing (ISC) with a rate k_{es}. From the shelving state, the population returns to the ground state with a rate k_{sg}. From the shelving state, the population preferentially populates the $| \pm 1/2\rangle$ spin substates. The resulting population difference of up to 80% [5] makes ODMR measurements possible. Writing n_g, n_e, and n_s for the populations of the electronic ground state $|G\rangle$, excited state $|E\rangle$, and shelving state $|S_1\rangle$, respectively, the population

dynamics can be written as

$$\frac{d}{dt}\vec{n} = \frac{d}{dt}\begin{pmatrix} n_g \\ n_e \\ n_s \end{pmatrix} = \begin{pmatrix} -k_{ge} & k_{eg} & k_{sg} \\ k_{ge} & -k_{eg} - k_{es} & \\ & k_{es} & -k_{sg} \end{pmatrix}\vec{n}. \quad (2)$$

The eigenvectors $\vec{v}_i$ are given in Appendix D and the eigenvalues for Eq. (2) are

$$\vec{\lambda} = \frac{1}{2}\begin{pmatrix} 0 \\ A + \sqrt{A^2 - 4B} \\ A - \sqrt{A^2 - 4B} \end{pmatrix}, \quad (3)$$

where $A = k_{ge} + k_{eg} + k_{es} + k_{sg}$ and $B = k_{sg}(k_{eg} + k_{es} + k_{ge}) + k_{es}k_{ge}$. The resulting stationary state is

$$\vec{n}^{st} = \frac{1}{B}\begin{pmatrix} k_{sg}(k_{eg} + k_{es}) \\ k_{ge}k_{sg} \\ k_{es}k_{ge} \end{pmatrix}. \quad (4)$$

To calculate the theoretical correlation function $g^2(\tau)$, we need the excited-state population at time τ when the system is initially in the ground state [$n_g(0) = 1$ and $n_e(0) = n_s(0) = 0$],

$$\frac{n_e(t)}{n_e^{st}} \overset{t=\tau}{=} g^{(2)}(\tau) = 1 - (1+c)e^{-\tau/\tau_1} + c\,e^{-\tau/\tau_2}, \quad (5)$$

with the inverse of the eigenvalues

$$\tau_{1,2} = 2/(A \pm \sqrt{A^2 - 4B}) \quad (6)$$

and the bunching amplitude

$$c = \frac{1 - \tau_2 k_{sg}}{k_{sg}(\tau_2 - \tau_1)}. \quad (7)$$

In Fig. 3, the solid dark-red lines are the fitted curves obtained using Eq. (5). In Fig. 5, we plot the extracted fit parameters τ_1, τ_2, and c vs the laser intensity. The experimental data points are compared to theoretical curves that can be obtained from the intensity dependence of the effective rate coefficients,

$$k_{sg} = \frac{1}{(1 + c^\infty)\tau_2^\infty},$$
$$k_{es} = k_{sg}c^\infty,$$
$$k_{eg} = \frac{1}{\tau_1^0} - k_{23}\ (k_{eg} + k_{es}) > k_{sg}, \quad (8)$$

where the values with superscript 0 refer to the low-intensity limit and those with superscript ∞ to the high-intensity limit [19,30]. The absorption cross section σ was obtained from the transition rate k_{ge} from the ground state to the excited state,

$$\sigma = \frac{h\nu}{I}\left(\frac{k_{ge}}{n_g}\right), \quad$$

with the population n_g of the ground state and $I/h\nu$ the number of incident photons per second per unit area. At saturation intensity I_0, the population n_g drops to $1/2$:

$$\frac{k_{ge}}{n_g(\infty)} = \frac{k_{sg}(k_{eg} + k_{es})}{k_{sg} + k_{eg}}. \quad (9)$$
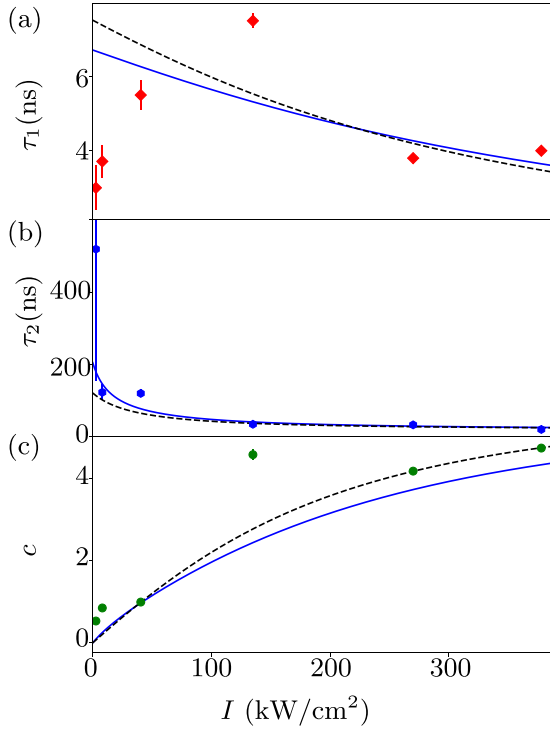
FIG. 5. Time constants τ_1, τ_2 and bunching amplitude c of the second-order correlation function for various laser-power intensities. The experimental data are fitted with the functions of Eqs. (3) and (7). All three datasets are fitted simultaneously, which results in the following parameters: $\tau_1^0 = (7.5 \pm 1.1)$ ns, $\tau_2^\infty = (17.2 \pm 1.4)$ ns, and $c^\infty = 6.0 \pm 0.5$ for the three-level model (black dashed curves); $\tau_1^0 = (6.7 \pm 1.4)$ ns, $\tau_2^0 = (204.4 \pm 166.3)$ ns, $\tau_2^\infty = (14.9 \pm 3.4)$ ns, and $c^\infty = 6.3 \pm 0.9$ for the four-level model (blue curves).

The absorption cross section can be written as

$$\sigma = \frac{k_{ge}}{n_g} \frac{h\nu}{I_0} = \frac{k_{sg}(k_{eg} + k_{es})}{k_{sg} + k_{es}} \frac{h\nu}{I_0},$$

fitting simultaneously the obtained values of $\tau_1^0 = (7.5 \pm 1.1)$ ns, $\tau_2^\infty = (17.2 \pm 1.4)$ ns, and $c^\infty = 6.0 \pm 0.5$ from the data plotted in Fig. 5 after simultaneously fitting in Eqs. (3) and (7). As in previous works [19,30], the three-level model well describes the antibunching decay time constant τ_1 [the black dashed line in Fig. 5(a)] and the bunching amplitude $c(I)$ [the black dashed line in Fig. 5(c)]. Table I shows the calculated rates and absorption cross section obtained from Eqs. (8). For low intensity ($I < 104\,\text{kW/cm}^2$), the bunching time constant reaches several-hundred ns, which is much longer than the window considered in Fig. 3. At higher inten-

TABLE I. Inverse rate coefficients and absorption cross section of the V_{Si}^- center.

Model	Inverse rate coefficients in ns				Cross section
	$1/k_{eg}$	$1/k_{es}$	$1/k_{sg}^0$	$1/k_{sg}^\infty$	σ (10^{-16} cm^2)
3 levels	12 ± 3	20 ± 2		120 ± 13	1.1 ± 0.2
4 levels	11 ± 4	17 ± 8	204 ± 166	15 ± 3	4.9 ± 1.2

sities, the bunching time gets shorter. In Refs. [19,30], this is explained as a deshelving process that can be described as shown in Fig. 4: The laser reexcites the system from the shelving state $|S_1\rangle$ to a higher-lying state $|S_2\rangle$ from where it can fall back to $|E\rangle$. The following are the rates for the four-level model:

$$k_{sg} = \frac{d\,I}{I + I_0} + k_{sg}^0,$$

$$k_{sg}^0 = \frac{1}{\tau_2^0},$$

$$k_{sg}^\infty = \frac{1}{\tau_2^\infty},$$

$$k_{es} = \frac{1}{\tau_2^\infty} - k_{sg}^0 - d,$$

$$k_{eg} = \frac{1}{\tau_1^0} - k_{es}, \qquad (10)$$

where $d = \frac{1/\tau_2^\infty - (1 + c^\infty)/\tau_2^0}{1 + c^\infty}$ [19,30]. Inclusion of the deshelving process results in the intensity-dependent rate from the shelving state to ground state k_{sg} [30], fitting simultaneously the obtained values of $\tau_1^0 = (6.7 \pm 1.4)$ ns, $\tau_2^0 = (204.4 \pm 166.3)$ ns, $\tau_2^\infty = (14.9 \pm 3.4)$ ns, and $c^\infty = 6.3 \pm 0.9$ from the data plotted in Fig. 5 after simultaneously fitting in Eqs. (3) and (7), using the four-level rates given in Eqs. (10). The blue curves in Fig. 5 correspond to the four-level model, which matches the experimental data better than the black dashed curves from the three-level model. We now compare our results to previous work [19], in which silicon vacancies were created through high-energy neutron irradiation without postannealing. The extracted transition times and cross sections from the four-level model were $1/k_{eg} = 7.6$ ns, $1/k_{es} = 16.8$ ns, $1/k_{sg}^0 = 150$ ns, $1/k_{sg}^\infty = 123$ ns, and $\sigma = 1.6 \times 10^{-16}$ cm^2 [19]. The transition times $1/k_{eg}$, $1/k_{es}$, and $1/k_{sg}^0$ measured by us for the shallow silicon-vacancy center are compatible, within the experimental uncertainties, with those of Fuchs *et al.* [19]. Further, the cross-section σ error bar's lower end is close to the cross section measured by Fuchs *et al.* [19]. The main difference between the two samples is the defect generation method and the depth of the center. We tentatively assign the defect generation method to the $\approx 5\times$ increase that we observed in our rate k_{sg}^∞. In our sample, emitters are created with low-energy helium ion implantation, followed by $600\,^\circ$C annealing to remove parasitic lattice damage. As has been shown in previous work [23], high damage defect generation can significantly alter radiative and nonradiative decay processes, which may modify relaxation rates [31]. Since our emitters are located within $\approx 40\,$nm at the surface, we additionally expect coupling to surface charge states and traps, which may lead to a symmetry reduction through which additional decay channels can be allowed. We believe that a more thorough analysis of the modification of the rates as a function of the defect generation method would be useful; however, this would require low-temperature experiments [32], which go beyond the scope of this paper.

Over the duration of the intensity-autocorrelation measurement, the count rate of the selected single center dropped
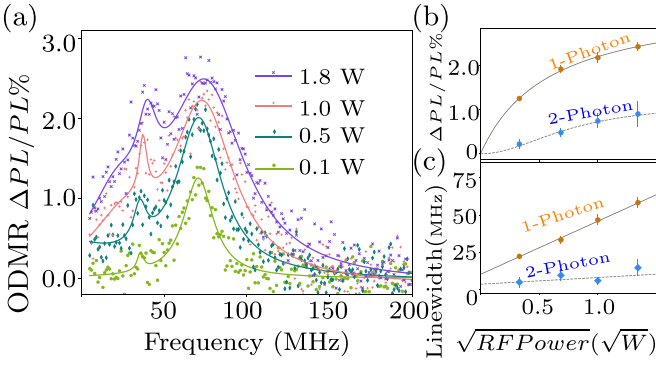
FIG. 6. (a) ODMR signal vs frequency recorded for center 2 with different RF powers in the absence of applied magnetic fields. The horizontal axis is the frequency in MHz, and the vertical axis is the relative change of the PL. (b) ODMR signal vs RF field strength, and (c) linewidth vs RF field strength.

significantly. We therefore used a different center (we call it center 2) for the ODMR experiment. The intensity-autocorrelation measurement data for that center confirm that it is also a single center.

IV. OPTICALLY DETECTED MAGNETIC RESONANCE

In conventional electron spin resonance (ESR), spins are measured by inductive detection, which limits the sensitivity of the technique. Using optical polarization of the spin system and optical detection, it is possible to sufficiently increase the sensitivity for experiments on single spins [33,34]. In this optically detected magnetic resonance (ODMR), the electron spin is excited with laser light to its optical excited state, and the PL emitted during reemission is detected while a radio-frequency (RF) or microwave (MW) field drives the spin system. The different spin states contribute differently to the PL rate, so that a change in the spin polarization leads to a change of the PL rate, which can be used to measure spin polarization. We used this technique for measuring the ODMR of a single silicon vacancy in 4H-SiC.

For recording the single center's continuous-wave (cw) ODMR, the center was continuously illuminated with an optimized laser intensity of 68 kW/cm^2 where the signal-to-background ratio is maximal; more details are given in Appendix F. The ODMR was recorded in "lock-in mode:" while stepping the RF over the relevant frequency range, PL counts were recorded with and without RF. The difference between the two values, $\Delta PL = PL_{RF} - PL_{off}$, is less sensitive to fluctuations of the laser intensity.

Figure 6(a) shows the recorded ODMR signal at different RF powers (0.1, 0.5, 1.0, and 1.8 W). The ODMR spectrum recorded with 0.1 W fitted in double Lorentzian function, and the obtained resonance frequencies are (72.8 ± 0.3) MHz for the main peak and (36.4 ± 0.2) MHz for the smaller peak. The frequency of the larger peak matches the literature value of the zero-field splitting of the V_2-type V_{Si}^- in 4H-SiC [27]. At high RF power, the Rabi frequency of the system is comparable to the resonance frequency of the system, and the rotating-wave approximation is no longer valid and causes nonlinear processes, such as multi-RF photon absorption [35]. In our

TABLE II. Obtained fitting parameters from Eq. (11) for the ODMR-signal amplitude and Eq. (12) for the linewidth vs RF field strength.

Peak	c	$S_{max}(\%)$	$\Lambda_0 (W^{c/2})$	Γ_0 (MHz)	a (MHz/$\sqrt{W}$)
1-photon	1	3.51 ± 0.25	0.59 ± 0.10	10.0 ± 2.3	35.9 ± 3.3
2-photon	2	1.2 ± 0.6	0.6 ± 0.6	$3.3^{-3.3}_{+4.0}$	5 ± 5

previous work [35], we studied the multi-RF process in detail. In those experiments, the large signal-to-noise ratio of the V_3 spin ensemble allowed detailed studies of the one-, two-, three-, and four-RF photon resonances. Here, the smaller peak is at half the frequency of the main peak, so we attribute it to the two-RF photon peak. In the simulated spectra shown in Appendix G [Fig. 13(a)], the multiphoton peaks are more clearly visible. In the experiment, the signals due to higher multiphoton absorption are not resolved due to the limited signal-to-noise ratio. To take these unresolved signal contributions into account, we add a third Lorentzian component to the fitting function of the ODMR spectra when the applied RF power is higher than 0.5 W. Figures 6(b) and 6(c) show the RF power dependence of the amplitudes and the linewidths for one- and two-photon peaks. The dependence of the amplitude is fitted with the function

$$S(P) = S_{max}[(P^{c/2}/(\Lambda_0 + P^{c/2})], \tag{11}$$

where $S(P)$ is the ODMR signal amplitude and P is the RF power. The exponent c is 1 (2) for the one- (two-)photon transitions [35]. The values for S_{max} and Λ_0 for the peaks are given in Table II.

The linewidth Γ vs the square root of the RF power, $\sqrt{P}$, is fitted to the function

$$\Gamma(P) = \Gamma_0 + a\sqrt{P}. \tag{12}$$

The obtained fitting parameters, intercept Γ_0, and slope a are given in Table II. The low-power limit Γ_0 corresponds to the inverse dephasing time $1/(\pi \Gamma_0)$ [36]. The low-power limit of the linewidth corresponds to a dephasing time of 32 ± 7 ns. One contribution to the linewidth is stray magnetic fields of about 0.5 G, which cause extra 2.8 MHz peak broadening. Apart from that, the contrast and the linewidth depend on the RF and laser intensity [37]. For the same kind of centers, $T_2^* = 34 \pm 4$ μs was measured at 10 K using Ramsey interferometry in an external magnetic field of $B_0 = 36$ G oriented along the crystal's c axis [23], and similar values were obtained in deep-bulk defects in similar SiC crystals [4,38]. Due to differences in experimental conditions between the present work and the study by Babin *et al.* [23], a quantitative comparison of the dephasing rates estimated here from the low-power limit, Γ_0, and the T_2^* measured in their study is not meaningful. However, it is worth considering some conditions contributing to the differences. Babin *et al.* performed their measurements at a low temperature of 10 K, while the measurements presented here were obtained at room temperature. Additionally, Babin *et al.* used the Ramsey method to measure free precession, whereas the present measurements were obtained using the cw method. Furthermore, in Babin *et al.*'s study, selective low-power resonant excitation ensured
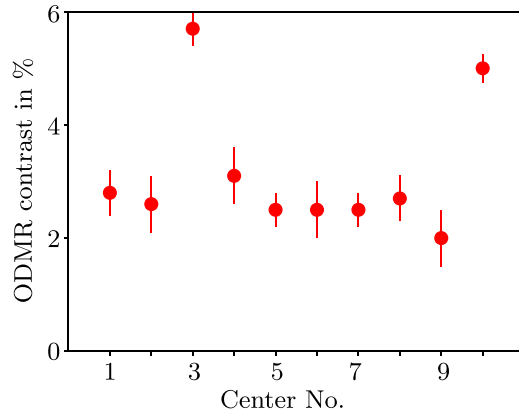
FIG. 7. ODMR contrast for different centers.

that the system was predominantly in the ground state. In contrast, in the present experiment, cw excitation led to the system being mostly in the metastable state, which contributes to the dephasing and line broadening. Lastly, Babin *et al.* applied a magnetic field to lift the degeneracy of the electron spin states, which reduces line broadening from magnetic field noise and changes the dynamics of the nuclear spin bath and its contribution to the line broadening [39]. Figure 13(b) of Appendix H shows the linewidth of the simulated spectra vs the RF coupling strength ($\Omega_1 = g\mu_B B_1$), which looks similar to the experimental data in Fig. 6(c). As shown in Fig. 13(b), the width of the two-photon resonance for low power tends to zero (which corresponds to $T_2^* \longrightarrow \infty$ for two-photon resonance) and the slope a_1 of the two-photon resonance is smaller than that of the one-photon resonance.

We recorded the ODMR of 10 more centers with 9 W RF power and 185 kW/cm^2 laser intensity. We observed the contrast range, and Fig. 7 shows the plot of the number of centers vs ODMR contrast. On average, we observed a $\approx 3\%$ contrast per center, with a minimum contrast of 1% and a maximum contrast of 6%. We also recorded ODMR spectra of one of the high contrast centers for the different RF and laser powers; more details are given in Appendix G.

V. DISCUSSION AND CONCLUSION

Vacancy centers in silicon carbide are useful tools for sensing magnetic fields and for other quantum technologies. With existing fabrication technology, V_{Si}^- can be produced on-demand with a high probability and reasonable resolution. Previously, the spin properties of a V_2 center deep inside a 4H-SiC sample have been studied using a solid immersion lens to enhance the PL of the V_2 center [3]. Here we characterized shallow single silicon-vacancy centers, which are very useful for quantum sensing applications. The single center is located approximately 40 nm below the surface and can be optically spin polarized; the measured optical transition rates are slightly different from the previously measured deep silicon-vacancy centers [3] and fitted well in the four-level model [19,30].

The dephasing rate of transition $\pm 3/2 \longleftrightarrow \pm 1/2$ was 32 ns. Longer dephasing times are expected for the $+1/2 \longleftrightarrow -1/2$ transition since it is not affected by the

zero-field splitting [7,17]; this may be interesting for sensing applications. Observing this transition is possible in an external magnetic field, which lifts the degeneracy of these levels and can result in a population imbalance between them. The maximum ODMR contrast of $\approx 6\%$ was obtained with 9 W RF power and 185 kW/cm^2 laser intensity.

To understand the exact cause of the difference between these transition rates and the ODMR contrast of the shallow and deep centers in our future work, we plan to perform experiments where we change the depth of the center, e.g., by the etching technique. Illumination for more than 24 hours with an intensity of 378 kW/cm^2 reduces the count rates. The reduced count rate may be due to charge state conversion [40]. Here we used a 785 nm laser, i.e., nonresonant pumping. It may be possible to avoid the reduction of the count rate by using a different laser wavelength close to the zero phonon line. We will try this approach in our future work.

In conclusion, we reported room-temperature ODMR data from single shallow V_{Si}^- centers in 4H-SiC. We observed higher ODMR contrast in the centers that were created with He$^+$ implantation than in previous studies where centers had been created by neutron irradiation [3,19,41]. Due to the higher contrast, we are able to record ODMR of a center with PL ≈ 8 kcps. An ensemble of V_{si}^- in SiC has a single dipole orientation, in contrast to an ensemble of NV centers in diamond with four possible dipole orientations. For some applications, this increases the signal by a factor of four. So, this increased ODMR contrast due to shallowness makes the silicon-vacancy center a good candidate as the NV center in diamonds for room-temperature sensing applications such as nuclear magnetic resonance of a small sample volume and magnetic resonance imaging of single cells [18,42–44].

APPENDIX A: SAMPLE

Arrays of V_{Si}^- centers via implantation of He$^+$ ions. He$^+$ ions were sent through a polymethyl methacryate (PMMA) mask with 100-nm-diameter holes, lithographed on the face of an epitaxially grown SiC sample with a low nitrogen concentration in the $[N] = 4 \times 10^{13}$ cm^{-3} range. The low He$^+$ ion energy of 6 keV was chosen to minimize the crystal damage.
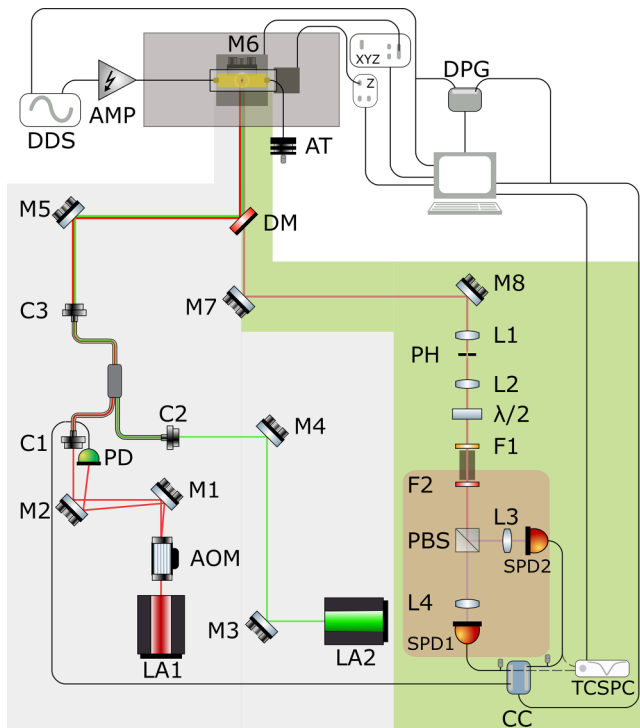
FIG. 8. Experimental confocal scan setup for the cw-ODMR (zfODMR), with intensity-autocorrelation and pulse measurements. The detectors are isolated in a box (reddish brown) to prevent noise from external light sources. PL can enter the box via a tube (between F1 and F2). Excitation path (gray background): the center is optically excited by a 785 nm laser. RF transitions are induced by a 50 μm copper wire over the sample. Detection path (green background): the PL is detected by two single-photon detectors (SPD1 and SPD2), which are connected to the DAQ card (DAQ) for ODMR measurements. When performing a g^2 measurement, the detectors are connected to the time-correlated single-photon counting (TCSPC) device (indicated by dashed lines).

To remove residual lattice damage, the sample was annealed in an argon atmosphere at 600 °C for 30 min [23]. Figure 2 shows the room-temperature PL map of an implanted array using off-resonant excitation at 785 nm.

APPENDIX B: ODMR SETUP

The excitation path (Fig. 8, gray background) begins with a 785 nm, 250 mW iBEAM-SMART-785-S-HP Laser (LA1) from Toptica, which induces electronic transitions of the $4H$-SiC system. The 520 nm Lasertack 100 mW single-mode diode laser (LA2) is used for alignment. Each laser beam is directed by two mirrors (M1 and M2/M3 and M4) and coupled by the Thorlabs fiberports (C1/C2) into a Thorlabs 532 nm/785 nm NG71F1 y-fiber which combines both beams. To perform pulse experiments, an acousto-optic modulator (AOM) is placed in front of the red laser (LA1). The zero-order beam is detected by a S2386-44K6K photodiode (Hamamatsu), which monitors the stability of the laser output. The first-order diffracted beam is coupled into the y-fiber. Finally, the combined laser beam is coupled out of the y-fiber by fiberport (C3) and directed by mirror (M5) to the DMLP805 long-pass dichroic mirror (DM) from Thorlabs,

which transmits wavelengths greater than 805 nm. Hence the combined light beam is reflected and directed by mirror (M6) into an Olympus UPLFLN100XO2 objective. It is mounted on a PI P-733.3CD *XYZ* nanopositioner which covers a range of 100 μm in the *X*, *Y* directions, and 10 μm in the *Z* direction. This *XYZ* nanopositioner is operated by a PI E-727 Digital Multichannel Piezo Controller. The combined laser beam is focused onto the sample which is mounted onto a circuit board, where RF fields are applied through a 50 μm copper wire. These RF fields are generated by an Analog Devices AD9915 2.5 GSPS Direct Digital Synthesiser (DDS). The RF power in the range 20–512 MHz can be increased for several watts by a 50 W Mini Circuit LZY-1 amplifier (AMP). It is important to connect a 50 Ω resistor at the other end of the circuit board to prevent damage of the electronic devices due to RF reflections. Since the resistor is limited to 1 W, the RF power is increased by an attenuator (AT) beforehand. The circuit board itself is screwed tight onto the sample stage that allows movements in the *Z* direction by a motorized Standa 8MT173 translation stage which is operated by the Standa 8SMC5-USB-B8-1 motor controller. In Fig. 8, the circuit board is shown in yellow, whereas the objective is illustrated as a circle below it. All components of the detection path (Fig. 8, green background) are selected for the near-infrared range of 805–1000 nm. PL emitted from the sample is collected by the microscope objective and directed by the mirror (M6) through the dichroic mirror (DM) (bright red line in Fig. 8). It is then directed by the mirrors (M7) and (M8) and focused by the lens (L1) with focal length of 100 mm, passes a 50 μm pinhole (PH), and is then collimated by the lens (L2) with a focal length of 150 mm. The following waveplate ($\lambda/2$) allows one to adjust the ratio between transmitted and reflected PL at the polarized beam splitter (PBS) in the box. Before entering the box via a tube, the PL is filtered by a 850 nm long-pass filter (F1). Depending on the type of measurement, a second filter (F2) like a (950 ± 25) nm band-pass filter or a 850 nm long-pass filter is used. The PL is split by the PBS and directed to the lens (L3/L4), each with focal length of 100 mm, which focuses the PL onto the Laser Components Count-100N single-photon detectors (SPD1 and SPD2, in which the photon detection efficiency at 810 nm is 68% and 59%). When performing an ODMR measurement, the registered events are counted by a Measurement Computing 1808X-USB DAQ-card (DAQ), which has a 50 Ω resistor at each input to prevent reflections. For intensity-autocorrelation measurements, we used time tagger and counters of QUPSI from quτools.

APPENDIX C: DETAILS OF INTENSITY-AUTOCORRELATION MEASUREMENTS

All but one of the g^2 measurements shown in Fig. 9 were taken with a bin width W_b of 486 ps, whereby the histogram data for $I = 378$ kW/cm^2 was obtained with W of 162 ps. Eventually, all unnormalized histogram datasets were normalized by $N_{\mathrm{norm}} = T \, W_b \, R_1 R_2$, with total time T, bin width W_b, and count rates R_i of the detectors D_i, and afterwards smoothed to a bin width of 972 ps. The total count rates $R = R_1 + R_2$ are obtained by dividing the total number of counts by the total time for the g^2 measurement. Finally,
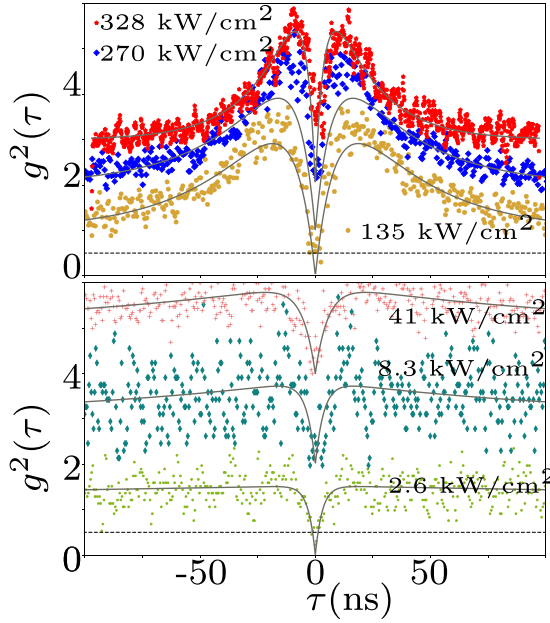
FIG. 9. Complete series of intensity-autocorrelation measurements performed from 2.6 kW/cm² to 378 kW/cm². The histogram data are first normalized by $N_{\rm norm} = {\rm T}\, W_b\, R_1\, R_2$ and then smoothed to a bin width of 972 ps. In addition, for the lowest $I = 2.6\,$kW/cm², all histogram datasets are corrected for their background. Each solid line follows the three-level correlation function from Eq. (5).

the individual count rates are then obtained by $R_1 = 0.6\,R$ and $R_2 = 0.4\,R$. At $I = 2.6\,$kW/cm², only the dark count rates of R_1, $D = 251\,$counts/s, and R_2, $D = 129\,$counts/s at each detector contribute to the background due to slightly different models. But a linear increase in background for increasing excitation power is observed in Fig. 10, which can be considered by applying a background correction. Since the background correction cannot be applied for a background which only consists of the detectors dark counts, it was applied on all histogram datasets except for the one at the lowest excitation powers of 2.6 kW/cm². Only the obtained normalized histogram data at smallest (orange diamond) and at
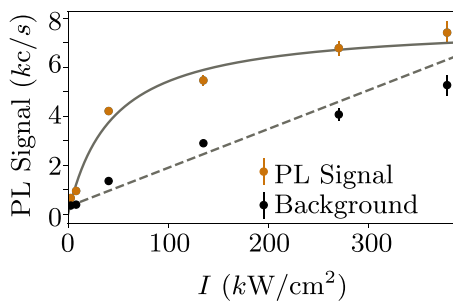

FIG. 10. PL signal at different intensities I of the center on which g^2 measurements were performed. The PL signal is fitted by $S = S_{\rm max} I/(I_0 + I)$ with (7.8 ± 0.3) k counts/s and $I_0 = (44 \pm 3)$ kW/cm², whereas the background increases linearly with the slope $m = (15.9 \pm 0.6)$ counts cm²/(kW s) and intercept b = (309 ± 20) counts/s.
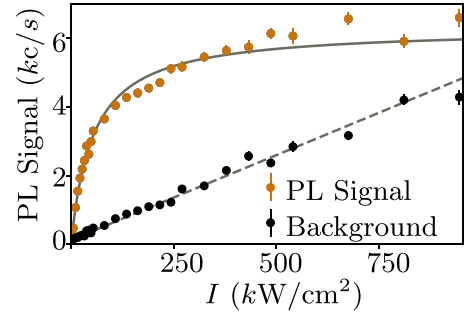

FIG. 11. PL signal at different intensities I. The PL signal is fitted by $S = S_{\rm max} I/(I_0 + I)$ with (6.3 ± 0.1) kcps and $I_0 = (53 \pm 2)$ kW/cm², whereas the background increases linearly with the slope $m = (4.9 \pm 0.1)$ counts cm²/(kW s) and intercept $b = (130 \pm 8)$ cps.

greatest (green star) optical excitation power are shown in Fig. 3. All histogram datasets are shown in Fig. 9.

APPENDIX D: EIGENVECTORS

Eigenvectors of the three-level model,

$$
\vec{v}_1 = \begin{pmatrix} 1 \\ \frac{k_{sg}}{k_{es}} \\ \frac{k_{sg}(k_{eg}+k_{es})}{k_{es}k_{ge}} \end{pmatrix},\
\vec{v}_2 = \begin{pmatrix} -1 \\ G \\ -F \end{pmatrix},\
\vec{v}_3 = \begin{pmatrix} -1 \\ -G \\ F \end{pmatrix},
$$

where

$$
\begin{aligned}
F &= \frac{H + k_{eg} - k_{es} + k_{ge} - k_{sg}}{2k_{es}}, \\
G &= \frac{H + k_{eg} + k_{es} + k_{ge} - k_{sg}}{2k_{es}}, \\
H &= \sqrt{k_{eg}^2 + 2k_{eg}(k_{es} + k_{ge} - k_{sg}) - J}, \\
J &= 2\,k_{sg}(k_{es} + k_{ge}) + (k_{es} - k_{ge})^2 + k_{sg}^2.
\end{aligned}
$$

APPENDIX E: OPTIMAL LASER POWER FOR ODMR

A suitable electronic excitation intensity I can be obtained from the saturation behavior of the PL signal. In Fig. 11, a maximum PL signal of (6.3 ± 0.1) kcps can be obtained, while the background increases linearly with increasing I. Therefore, $I_0 = (53 \pm 2)$ kW/cm² is chosen for ODMR measurements since the PL signal is almost saturated while the background is relatively small. Even if a high background is mostly compensated by the reference's detection ΔPL, it has the advantage that the autofocus works more reliably at low background.

APPENDIX F: ODMR SIMULATIONS

For the numerical simulation, we used the Lindblad master equation

$$
\frac{\partial \rho}{\partial t} = -2\pi i\, [\mathcal{H}_t(t), \rho] + \sum_{\alpha, \beta, \delta_{1,\dots,5}} L_i^\dagger \rho L_i - \frac{1}{2}\{L_i^\dagger L_i, \rho\},
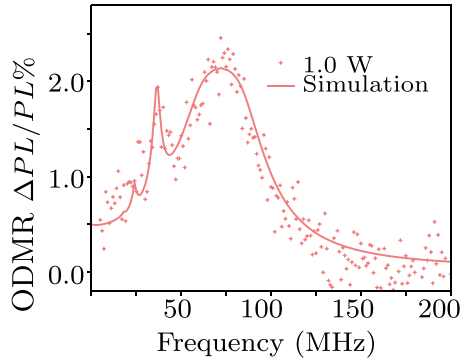$$

$$
\tag{F1}
$$

FIG. 12. Experimental and simulated ODMR plots for silicon vacancy with the RF Hamiltonian of Eq. (F1).

where

$$\mathcal{H}_t(t) = \mathcal{H} + \mathcal{H}_{RF}(t),$$

$$L_\alpha = \sqrt{2} \begin{pmatrix} 0 & \sqrt{\gamma} & 0 & 0 \\ \sqrt{\gamma} & 0 & \sqrt{\alpha} & 0 \\ 0 & \sqrt{\alpha} & 0 & \sqrt{\gamma} \\ 0 & 0 & \sqrt{\gamma} & 0 \end{pmatrix} \approx \sqrt{2\alpha}\, S_x$$

drives the spin-lattice relaxation process, $\gamma = 3\alpha/4$, $L_\beta = \sqrt{2\beta}\, S_z$ is the Lindblad operator for the dephasing process, and $L_{\delta_{1,\dots,5}}$ are the Lindblad operators for the optical pumping [35],

$$L_{\delta_1} = \sqrt{\delta}\begin{pmatrix} 0 & 0 & 0 & 0 \\ 1 & 0 & 0 & 0 \\ 0 & 0 & 0 & 0 \\ 0 & 0 & 0 & 0 \end{pmatrix}, \quad L_{\delta_2} = \sqrt{\delta}\begin{pmatrix} 0 & 0 & 0 & 0 \\ 0 & 0 & 0 & 1 \\ 0 & 0 & 0 & 0 \\ 0 & 0 & 0 & 0 \end{pmatrix},$$

$$L_{\delta_3} = \sqrt{\delta}\begin{pmatrix} 0 & 0 & 0 & 0 \\ 0 & 0 & 0 & 0 \\ 1 & 0 & 0 & 0 \\ 0 & 0 & 0 & 0 \end{pmatrix}, \quad L_{\delta_4} = \sqrt{\delta}\begin{pmatrix} 0 & 0 & 0 & 0 \\ 0 & 0 & 0 & 0 \\ 0 & 0 & 0 & 1 \\ 0 & 0 & 0 & 0 \end{pmatrix},$$

$$L_{\delta_5} = \sqrt{\delta}\begin{pmatrix} 0 & 0 & 0 & 0 \\ 0 & 0 & 1 & 0 \\ 0 & 1 & 0 & 0 \\ 0 & 0 & 0 & 0 \end{pmatrix},$$

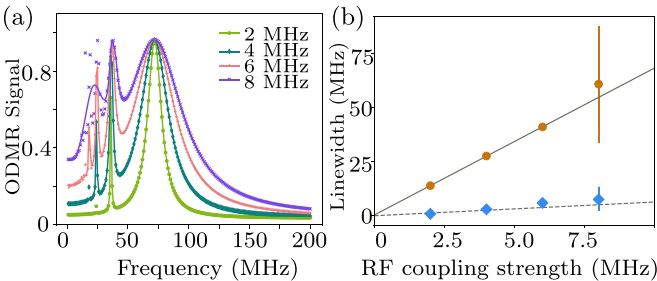and δ is the optical pumping rate [7].

FIG. 13. (a) Simulated ODMR spectra at different RF strengths. (b) Linewidth of one-photon and two-photon resonances vs RF coupling strength.
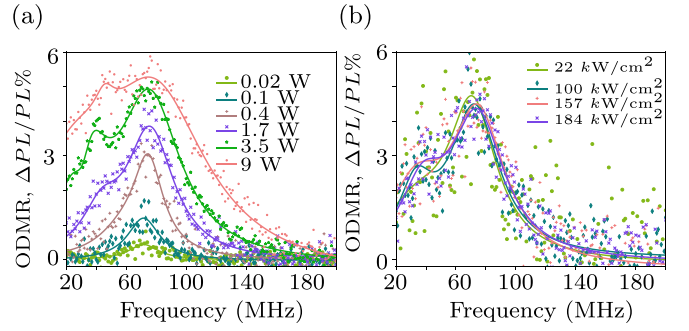

FIG. 14. ODMR spectra recorded for one of the high contrast centers (out of 10 measured centers), (a) with different applied RF power and $184\,\text{kW/cm}^2$ laser intensity, and (b) with different laser intensities and 2.6 W RF power. The horizontal axis is the frequency in MHz and the vertical axis is the relative change of the PL%.

The interaction Hamiltonian between the RF field and the spins is

$$\mathcal{H}_{RF}(t) = \Omega_1 \cos(2\pi\omega t)(S_x + S_z),$$

where $\Omega_1 = g\mu_B B_1$ represents the strength of the coupling to the RF field B_1 in frequency units and ω is the oscillation frequency of the field. Figure 12 shows the experimental and simulated ODMR spectra at 8 MHz RF coupling strengths with $\alpha = 7\,\text{ms}^{-1}$, $\beta = 10\,\mu\text{s}^{-1}$, and $\delta = 185\,\text{ms}^{-1}$; the simulated spectrum matches well with the experimentally recorded ODMR at 1 W RF power. Since we are using a simple optical pumping model [7], the amplitude of the simulated spectrum is normalized to the maximal ODMR contrast for the plot. For the simulated spectrum, we integrated Eq. (F1) for 1.5 μs for every frequency. Additional details can be found in our previous work [35]. Figure 13(a) shows the simulated ODMR spectra at different RF coupling strengths with the same parameters used for simulating the ODMR spectrum in Fig. 12, except for the value of β, which we reduced here to 2.5 μs^{-1} to better resolve the multiphoton peaks.

In Fig. 13, with an RF coupling strength of 2 MHz, we can see one-photon and two-photon peaks at 72 and 36 MHz and a small signal of a three-photon peak at 24 MHz. At 8 MHz, the five-, four-, and three-photon peaks are also visible and close to each other, and therefore difficult to resolve. The linewidth of the one- and two-photon peaks is extracted by fitting the simulated ODMR to a sum of Lorentzians. Figure 13(b) shows the resulting dependence of the linewidth Γ vs the RF coupling strength Ω_1 together with a fit to the function

$$\Gamma(P) = \Gamma_0 + a_1 \Omega_1. \tag{F2}$$

The obtained fitting parameters, intercept Γ_0, and slope a are given in Table III.

TABLE III. Obtained fitting parameters from Eq. (F2) for the linewidth vs RF field strength.

Peak	Γ_0 (MHz)	a
1	0.34 ± 0.21	6.80 ± 0.05
2	≈ 0	0.63 ± 0.05

APPENDIX G: ODMR WITH DIFFERENT RF AND LASER POWERS

Figure 14(a) shows the ODMR signal recorded for one of the high-contrast centers with different RF power, keeping the laser intensity at $184 \, \text{kW/cm}^2$ and Fig. 14(b) for different laser intensity at 2 W RF power. At 9 W RF power, the ODMR signal contrast is 5.3% and the laser intensity does not affect the ODMR contrast significantly. In the course of recording these data, the PL count of the center fell from 8 to 4 kcps, which impacts the signal-to-noise ratio of the later-recorded variable laser intensity ODMR spectra.

[1] W. F. Koehl, B. B. Buckley, F. J. Heremans, G. Calusine, and D. D. Awschalom, Room temperature coherent control of defect spin qubits in silicon carbide, Nature (London) **479**, 84 (2011).

[2] H. Kraus, V. A. Soltamov, D. Riedel, S. Väth, F. Fuchs, A. Sperlich, P. G. Baranov, V. Dyakonov, and G. V. Astakhov, Room-temperature quantum microwave emitters based on spin defects in silicon carbide, Nat. Phys. **10**, 157 (2014).

[3] M. Widmann, S.-Y. Lee, T. Rendler, N. T. Son, H. Fedder, S. Paik, L.-P. Yang, N. Zhao, S. Yang, I. Booker *et al.*, Coherent control of single spins in silicon carbide at room temperature, Nat. Mater. **14**, 164 (2015).

[4] R. Nagy, M. Niethammer, M. Widmann, Y.-C. Chen, P. Udvarhelyi, C. Bonato, J. U. Hassan, R. Karhu, I. G. Ivanov, N. T. Son *et al.*, High-fidelity spin and optical control of single silicon-vacancy centres in silicon carbide, Nat. Commun. **10**, 1954 (2019).

[5] V. A. Soltamov, A. A. Soltamova, P. G. Baranov, and I. I. Proskuryakov, Room Temperature Coherent Spin Alignment of Silicon Vacancies in 4*H*- and 6*H*-SiC, Phys. Rev. Lett. **108**, 226402 (2012).

[6] D. Riedel, F. Fuchs, H. Kraus, S. Väth, A. Sperlich, V. Dyakonov, A. A. Soltamova, P. G. Baranov, V. A. Ilyin, and G. V. Astakhov, Resonant Addressing and Manipulation of Silicon Vacancy Qubits in Silicon Carbide, Phys. Rev. Lett. **109**, 226402 (2012).

[7] H. Singh, A. N. Anisimov, I. D. Breev, P. G. Baranov, and D. Suter, Optical spin initialization of spin-$\frac{3}{2}$ silicon vacancy centers in 6*H*-SiC at room temperature, Phys. Rev. B **103**, 104103 (2021).

[8] S. G. Carter, Ö. O. Soykal, P. Dev, S. E. Economou, and E. R. Glaser, Spin coherence and echo modulation of the silicon vacancy in $4H - \text{SiC}$ at room temperature, Phys. Rev. B **92**, 161202(R) (2015).

[9] D. Simin, H. Kraus, A. Sperlich, T. Ohshima, G. V. Astakhov, and V. Dyakonov, Locking of electron spin coherence above 20 ms in natural silicon carbide, Phys. Rev. B **95**, 161201(R) (2017).

[10] D. J. Christle, A. L. Falk, P. Andrich, P. V. Klimov, J. U. Hassan, N. T. Son, E. Janzén, T. Ohshima, and D. D. Awschalom, Isolated electron spins in silicon carbide with millisecond coherence times, Nat. Mater. **14**, 160 (2015).

[11] H. Singh, A. N. Anisimov, S. S. Nagalyuk, E. N. Mokhov, P. G. Baranov, and D. Suter, Experimental characterization of spin-$\frac{3}{2}$ silicon vacancy centers in 6*H*-SiC, Phys. Rev. B **101**, 134110 (2020).

[12] I. Lekavicius, R.L. Myers-Ward, D.J. Pennachio, J.R. Hajzus, D.K. Gaskill, A.P. Purdy, A.L. Yeats, P.G. Brereton, E.R. Glaser, T.L. Reinecke, and S.G. Carter, Orders of magnitude improvement in coherence of silicon-vacancy ensembles in isotopically purified 4H-SiC, PRX Quantum **3**, 010343 (2022).

[13] P. Udvarhelyi, G. Thiering, N. Morioka, C. Babin, F. Kaiser, D. Lukin, T. Ohshima, J. Ul-Hassan, N. T. Son, J. Vučković, J. Wrachtrup, and A. Gali, Vibronic States and Their Effect on the Temperature and Strain Dependence of Silicon-Vacancy Qubits in 4*H*-SiC, Phys. Rev. Appl. **13**, 054017 (2020).

[14] Z. Shang, A. Hashemi, Y. Berencén, H.-P. Komsa, P. Erhart, S. Zhou, M. Helm, A. V. Krasheninnikov, and G. V. Astakhov, Local vibrational modes of Si vacancy spin qubits in SiC, Phys. Rev. B **101**, 144109 (2020).

[15] A. Anisimov, D. Simin, V. A. Soltamov, S. P. Lebedev, P. G. Baranov, G. V. Astakhov, and V. Dyakonov, Optical thermometry based on level anticrossing in silicon carbide, Sci. Rep. **6**, 33301 (2016).

[16] J. B. S. Abraham, C. Gutgsell, D. Todorovski, S. Sperling, J. E. Epstein, B. S. Tien-Street, T. M. Sweeney, J. J. Wathen, E. A. Pogue, P. G. Brereton, T. M. McQueen, W. Frey, B. D. Clader, and R. Osiander, Nanotesla Magnetometry with the Silicon Vacancy in Silicon Carbide, Phys. Rev. Appl. **15**, 064022 (2021).

[17] V. A. Soltamov, C. Kasper, A. V. Poshakinskiy, A. N. Anisimov, E. N. Mokhov, A. Sperlich, S. A. Tarasenko, P. G. Baranov, G. V. Astakhov, and V. Dyakonov, Excitation and coherent control of spin qudit modes in silicon carbide at room temperature, Nat. Commun. **10**, 1678 (2019).

[18] J. M. Taylor, P. Cappellaro, L. Childress, L. Jiang, D. Budker, P. Hemmer, A. Yacoby, R. Walsworth, and M. Lukin, High-sensitivity diamond magnetometer with nanoscale resolution, Nat. Phys. **4**, 810 (2008).

[19] F. Fuchs, B. Stender, M. Trupke, D. Simin, J. Pflaum, V. Dyakonov, and G. Astakhov, Engineering near-infrared single-photon emitters with optically active spins in ultrapure silicon carbide, Nat. Commun. **6**, 7578 (2015).

[20] T. C. Hain, F. Fuchs, V. A. Soltamov, P. G. Baranov, G. V. Astakhov, T. Hertel, and V. Dyakonov, Excitation and recombination dynamics of vacancy-related spin centers in silicon carbide, J. Appl. Phys. **115**, 133508 (2014).

[21] C. Kasper, D. Klenkert, Z. Shang, D. Simin, A. Gottscholl, A. Sperlich, H. Kraus, C. Schneider, S. Zhou, M. Trupke, W. Kada, T. Ohshima, V. Dyakonov, and G. V. Astakhov, Influence of Irradiation on Defect Spin Coherence in Silicon Carbide, Phys. Rev. Appl. **13**, 044054 (2020).

[22] T. Hornos, A. Gali, and B. G. Svensson, Large-scale electronic structure calculations of vacancies in 4*H*-SiC using the Heyd-Scuseria-Ernzerhof screened hybrid density functional, in *Silicone Carbide and Related Materials 2010*, Materials Science Forum, edited by E. V. Monakhov, T. H. Bengt, and G. Svensson (Trans Tech Publications Ltd., Durnten-Zurich, Switzerland, 2011), Vol. 679, pp. 261–264.

[23] C. Babin, R. Stöhr, N. Morioka, T. Linkewitz, T. Steidl, R. Wörnle, D. Liu, E. Hesselmeier, V. Vorobyov, A. Denisenko *et al.*, Fabrication and nanophotonic waveguide integration of silicon carbide colour centres with preserved spin-optical coherence, Nat. Mater. **21**, 67 (2022).

[24] J. Wang, X. Zhang, Y. Zhou, K. Li, Z. Wang, P. Peddibhotla, F. Liu, S. Bauerdick, A. Rudzinski, Z. Liu *et al.*, Scalable fabrication of single silicon vacancy defect arrays in silicon carbide using focused ion beam, ACS Photon. **4**, 1054 (2017).

[25] S. P. Pavunny, A. L. Yeats, H. B. Banks, E. Bielejec, R. L. Myers-Ward, M. T. DeJarld, A. S. Bracker, D. K. Gaskill, and S. G. Carter, Arrays of Si vacancies in 4*H*-SiC produced by focused Li ion beam implantation, Sci. Rep. **11**, 3561 (2021).

[26] V. Ivády, J. Davidsson, N. T. Son, T. Ohshima, I. A. Abrikosov, and A. Gali, Identification of Si-vacancy related room-temperature qubits in 4*H* silicon carbide, Phys. Rev. B **96**, 161114(R) (2017).

[27] P. G. Baranov, A. P. Bundakova, A. A. Soltamova, S. B. Orlinskii, I. V. Borovykh, R. Zondervan, R. Verberk, and J. Schmidt, Silicon vacancy in SiC as a promising quantum system for single-defect and single-photon spectroscopy, Phys. Rev. B **83**, 125203 (2011).

[28] A. M. Fox, M. Fox *et al.*, *Quantum Optics: An Introduction* (Oxford University Press, Oxford, 2006), Vol. 15.

[29] T. Basché, W. E. Moerner, M. Orrit, and H. Talon, Photon Antibunching in the Fluorescence of a Single Dye Molecule Trapped in a Solid, Phys. Rev. Lett. **69**, 1516 (1992).

[30] E. Neu, D. Steinmetz, J. Riedrich-Möller, S. Gsell, M. Fischer, M. Schreck, and C. Becher, Single photon emission from silicon-vacancy colour centres in chemical vapour deposition nano-diamonds on iridium, New J. Phys. **13**, 025012 (2011).

[31] C. A. Kasper, Engineering of highly coherent silicon vacancy defects in silicon carbide, Ph.D. thesis, Universität Würzburg, 2021.

[32] N. Morioka, D. Liu, O. O. Soykal, I. Gediz, C. Babin, R. Stöhr, T. Ohshima, N. T. Son, J. Ul-Hassan, F. Kaiser, and J. Wrachtrup, Spin-Optical Dynamics and Quantum Efficiency of a Single V1 Center in Silicon Carbide, Phys. Rev. Appl. **17**, 054005 (2022).

[33] D. Suter, Optical detection of magnetic resonance, Magn. Reson. **1**, 115 (2020).

[34] D. Suter and F. Jelezko, Single-spin magnetic resonance in the nitrogen-vacancy center of diamond, Prog. Nucl. Magn. Reson. Spectrosc. **98**, 50 (2017).

[35] H. Singh, M. A. Hollberg, A. N. Anisimov, P. G. Baranov, and D. Suter, Multi-photon multi-quantum transitions in the spin-$\frac{3}{2}$ silicon-vacancy centers of sic, Phys. Rev. Res. **4**, 023022 (2022).

[36] J. Wertz, *Electron Spin Resonance: Elementary Theory and Practical Applications* (Springer Science & Business Media, New York, 2012).

[37] K. Jensen, V. M. Acosta, A. Jarmola, and D. Budker, Light narrowing of magnetic resonances in ensembles of nitrogen-vacancy centers in diamond, Phys. Rev. B **87**, 014115 (2013).

[38] A. Bourassa, C. P. Anderson, K. C. Miao, M. Onizhuk, H. Ma, A. L. Crook, H. Abe, J. Ul-Hassan, T. Ohshima, N. T. Son *et al.*, Entanglement and control of single nuclear spins in isotopically engineered silicon carbide, Nat. Mater. **19**, 1319 (2020).

[39] O. Bulancea-Lindvall, N. T. Son, I. A. Abrikosov, and V. Ivády, Dipolar spin relaxation of divacancy qubits in silicon carbide, npj Comput. Mater. **7**, 213 (2021).

[40] G. Wolfowicz, C. P. Anderson, A. L. Yeats, S. J. Whiteley, J. Niklas, O. G. Poluektov, F. J. Heremans, and D. D. Awschalom, Optical charge state control of spin defects in 4*H*-SiC, Nat. Commun. **8**, 1876 (2017).

[41] J.-F. Wang, Q. Li, F.-F. Yan, H. Liu, G.-P. Guo, W.-P. Zhang, X. Zhou, L.-P. Guo, Z.-H. Lin, J.-M. Cui *et al.*, On-demand generation of single silicon vacancy defects in silicon carbide, ACS Photon. **6**, 1736 (2019).

[42] D. R. Glenn, K. Lee, H. Park, R. Weissleder, A. Yacoby, M. D. Lukin, H. Lee, R. L. Walsworth, and C. B. Connolly, Single-cell magnetic imaging using a quantum diamond microscope, Nat. Methods **12**, 736 (2015).

[43] D. R. Glenn, D. B. Bucher, J. Lee, M. D. Lukin, H. Park, and R. L. Walsworth, High-resolution magnetic resonance spectroscopy using a solid-state spin sensor, Nature (London) **555**, 351 (2018).

[44] D. B. Bucher, D. R. Glenn, H. Park, M. D. Lukin, and R. L. Walsworth, Hyperpolarization-Enhanced NMR Spectroscopy with Femtomole Sensitivity using Quantum Defects in Diamond, Phys. Rev. X **10**, 021053 (2020).